Anal Bioanal Chem (2012) 403:1415–1432
DOI 10.1007/s00216-012-5836-7

ORIGINAL PAPER

Chain-length-identification strategy in zinc polyphosphate glasses by means of XPS and ToF-SIMS

Maura Crobu · Antonella Rossi · Filippo Mangolini · Nicholas D. Spencer

Received: 10 September 2011 / Revised: 29 January 2012 / Accepted: 3 February 2012 / Published online: 27 March 2012

Abstract The surface chemistry of amorphous zinc polyphosphates of different compositions (ranging from zinc metaphosphate to zinc orthophosphate) has been investigated by means of X-ray photoelectron spectroscopy (XPS) and time-of-flight secondary-ion mass spectroscopy (ToF-SIMS). The identification of the chain length of zinc polyphosphates by XPS was on the basis of the integrated intensity ratio of the bridging (P–O–P) and nonbridging (P=O and P–O–M) oxygen peaks used for fitting the oxygen 1s signal, the shift of the P $2p_{3/2}$ signal towards lower binding energies and the modified Auger parameter towards higher values as the zinc content increases. The discrimination of the polyphosphate chain lengths was also achieved by ToF-SIMS, by comparing the intensities of selected characteristic phosphate fragments. Both techniques appear to be suitable for the investigation of polyphosphate glasses in applications such as tribology, where there is a need to identify the chain length present in the outermost monolayer of the film. Fourier-transform infrared (FT-IR) spectroscopy was used to characterize the bulk compounds. The FT-IR studies showed that long-chain structures linked through P–O–P bonds predominate in the metaphosphate composition, while when the zinc content is increased, the chains become shorter, ultimately being replaced by PO_4 monomers in the orthophosphate composition.

Keywords Polyphosphate glasses · X-ray photoelectron spectroscopy · Time-of-flight secondary-ion mass spectroscopy · Fourier transform IR spectroscopy

Introduction

Polyphosphate glasses consist of cross-linked networks, whose building blocks are phosphate tetrahedra. By linking through covalent bridging oxygen (BO) atoms, these tetrahedra can form various polyphosphate species [1, 2]. In the case of phosphorus pentoxide (P_2O_5), there are three tetrahedral linkages (i.e., three oxygen atoms covalently bind the phosphate tetrahedra), leaving, as a consequence, one terminal oxygen (P=O) present in the network. On the basis of the number of BO atoms, the tetrahedra present in P_2O_5 are therefore classified as Q_3 (see Fig. 1). When a modifying oxide is added to P_2O_5, the network is depolymerized as a consequence of the substitution of P–O–P bonds by P–O–M bonds (with M being a metal). Thus, a wide range of compositions and structures can be obtained depending on the metal oxide to P_2O_5 ratio , i.e., the oxygen-to-phosphorus ratio, [O]/[P] [1, 3, 4]. When [O]/[P] is 3, the structure is characterized by long chains consisting of Q_2 tetrahedra (i.e., phosphate tetrahedra sharing two oxygen atoms): this is known as the metaphosphate region. Changing to higher oxide content, the average chain length decreases, resulting, eventually, in Q_1 dimers (pyrophosphate, [O]/[P] of 3.5) and Q_0 monomers (orthophosphate, [O]/[P] of 4) [5–7].

Electronic supplementary material The online version of this article (doi:10.1007/s00216-012-5836-7) contains supplementary material, which is available to authorized users.

M. Crobu · A. Rossi · F. Mangolini · N. D. Spencer (✉)
Laboratory for Surface Science and Technology,
Department of Materials, ETH Zurich,
Wolfgang-Pauli-Strasse 10,
8093 Zurich, Switzerland
e-mail: nspencer@ethz.ch

A. Rossi (✉)
Dipartimento di Chimica Inorganica ed Analitica,
Università degli Studi di Cagliari, INSTM Unit,
Cittadella Universitaria di Monserrato,
09100 Cagliari, Italy
e-mail: rossi@unica.it

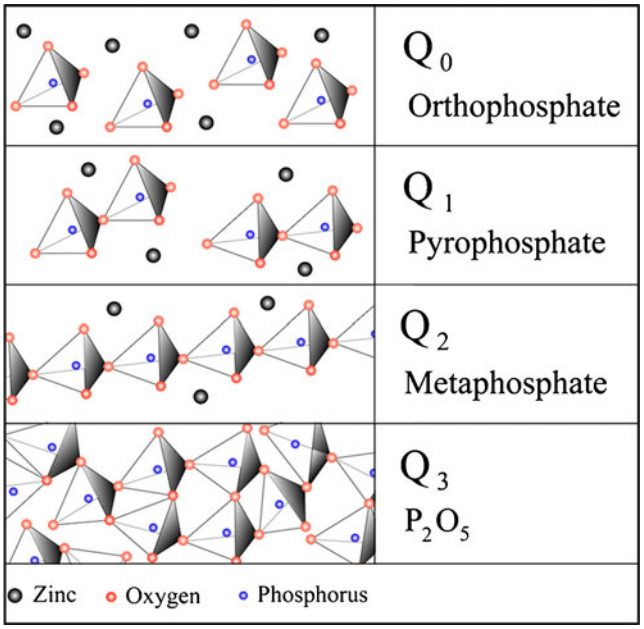

Fig. 1 Terminology for different composition and structures in polyphosphate glasses

The possibility of synthesizing zinc polyphosphate glasses over a wide compositional range is the main reason why they have often been chosen, among many other different binary phosphates glasses, for detailed structural studies. Zinc phosphate glasses show a discontinuity in the composition-property dependence of the refractive index, mass density, and glass-transition temperature in the transition from ultraphosphate to polyphosphate composition [8, 9]. It has been observed, for example, that the glass-transition temperatures values go through a minimum between metaphosphate and pyrophosphate composition. A change in coordination of the Zn^{2+} cation from 4 to 6 at the metaphosphate composition has been hypothesized as an explanation for this anomalous behavior, which is in common only with that of magnesium phosphate glasses. However, this theory has not been supported by experiment. In contrast, the Zn coordination number was found to be nearly constant with the composition, with an average value of 4 [8–13]. Raman spectroscopy [3, 14], infrared (IR) spectroscopy [14–18], and nuclear magnetic resonance (NMR) spectroscopy [5, 7, 19] have been commonly employed for studying the structure of polyphosphates.

Research on polyphosphate glasses has recently been stimulated by a wide range of technical uses of these compounds. The materials are good candidates for various optical applications, such as optical waveguides and high-power lasers. They have been considered as materials for nuclear-waste immobilization and, thanks to their very high thermal expansion coefficient, as materials for hermetic seals. Phosphate-based glasses have unique dissolution properties in aqueous-based fluids: The P–O–P linkages present in the glass networks can be easily hydrolyzed [20], which results in poor water durability, limiting, therefore, the possible practical uses of those materials. On the other hand, this poor chemical durability to hydrolysis makes these compounds useful as bioactive functional materials in applications such as hard and soft tissue engineering and controlled-release glasses [21]. The introduction of dopants can also be used for tuning their biocompatibility [22], their biological functionalities [21], and for improving their chemical durability [23].

Polyphosphate glasses have also been found to be responsible for the good antiwear properties of phosphorus-based engine-oil additives [24–26]. These additives are able to react at the interface between two sliding surfaces to form a reaction film, the so-called tribofilm. In the field of tribology, the hope of understanding the antiwear mechanism of phosphorus-based additives has led to renewed interest in investigating the mechanical and tribochemical properties of zinc and iron polyphosphates [27, 28]. The films formed on tribostressed surfaces generally have a thickness ranging from a few nanometers to 200 nm, and for this reason the application of surface analytical techniques to the characterization of polyphosphate glasses is very important.

A relevant contribution to the understanding of the formation of glassy tribofilm polyphosphates has been provided by the application of many surface-analytical techniques, such as X-ray photoelectron spectroscopy (XPS) [24, 29, 30], Auger electron spectroscopy [31], and X-ray absorption near-edge spectroscopy (XANES) [32]. The analytical questions to be addressed when chemical reactions are occurring at a surface under mechanical stress are many and various, but all are crucial. Not only it is required to identify the elements, the nature of the chemical bonds, and the thickness and composition of layers—very often only a few nanometers thick—but also knowledge of the composition in both in the lateral and the vertical direction is needed, if possible obtained in a nondestructive way. To date there is no single technique that provides all this information, and only the combined application of different spectroscopies can help in understanding the surface chemistry of challenging systems such as those characteristic of tribology. XPS is one of the most versatile techniques, since it allows identification of the elements (except H and He), it provides information on the chemical bonds between the elements, and, under certain circumstances, it can provide the thickness and composition even of multilayer systems, resolving the surface composition in the nanometer range [33, 34]. Auger electron spectroscopy is unique for its high lateral resolution, which may reach a few tens of nanometers, but it fails in providing information at the molecular level, and problems may arise if the films are not conductive. XANES has also been applied for the determination of polyphosphate chain lengths [32]. This spectroscopy, in total electron yield and fluorescence yield detection modes at the P K-edge, provides information that is averaged over sampling depths that have been estimated as

5 nm and about 60 nm, respectively, with a lateral resolution of 500 nm [32]. A practical limitation of its applicability is that it relies on synchrotron radiation. An extensive XANES investigation of chain lengths has been published for sodium polyphosphate glasses [35].

XPS analysis of phosphate glasses was first performed in the 1970s. It was observed that the O 1*s* signal could be curve-fitted with two components: the first component was assigned to the bridging P–O–P oxygen atoms (BO atoms), whereas the second component included two kinds of terminal oxygen atoms, P=O and P–O–M. Since the chemical shift between these latter two signals, i.e., P=O and P–O–M, is small and, therefore, they cannot be distinguished by any XPS spectrometer, a single peak, labeled as nonbridging oxygen (NBO), is usually used in XPS curve-fitting procedures [36, 37]. The identification of the chain length in polyphosphate glasses, including some binary zinc phosphates [6, 38, 39], on the basis of the BO/NBO ratio has been extensively reported in the literature [30, 40–48]. However, the quantification of the BO/NBO ratio is easily affected by the presence of contaminants. Another practical limitation is the dramatic change induced in the glass surface composition by ion-beam sputtering, which is commonly used to obtain contamination-free surfaces for XPS analysis or to obtain sputtering depth profiles [49]. Previous studies have also shown that the P 2*p* binding energy (BE) is dependent on the metal oxide content of the glass [43].

Complementary information to that provided by the core-electron photoelectronic signals can be obtained by investigating the valence-band region and the Auger signals. The valence-band region allows chemical information to be obtained that cannot be identified by the core levels [50]. A few studies have already shown that the XPS valence band can be used to distinguish oxides from phosphate compounds and also to differentiate between different phosphates [51, 52]. Another powerful tool for obtaining important chemical information is the Auger parameter and its representation in the so-called Wagner plot [51]. The use of such tools provides the ability to identify chemical states unequivocally and to learn about the local chemical environment of core-ionized atoms [53–55].

Time-of-flight (ToF) secondary-ion mass spectroscopy (SIMS) can provide molecular information combining an excellent lateral resolution (on the order of 100 nm) with a sampling depth of a monolayer. Furthermore, ToF-SIMS also has the unique ability to identify hydrogen-containing molecules. This latter characteristic will turn out to be very useful when the method proposed here for chain-length determination is applied to real systems, which very often may contain hydrogen as a cation. ToF-SIMS imaging of elements (Zn, Fe, Ca, P, S) and low-mass ions (PO, PO_2, PO_3) has already been successfully applied to tribological samples [56–59]. Murase and Ohmori investigated [60] the adsorption and reaction of phosphate-type lubricant additives (zinc- and sulfur-free) on ferrous materials by ToF-SIMS. The capabilities of such a technique have not been pushed to the limits in tribology so far. The recent introduction of polyatomic primary ion sources has been found to improve the yield of secondary ions, reducing the surface damage compared with that for monoatomic sources. In this way it is possible to eject and detect high-mass molecular fragments with good signal-to-noise ratio. This approach has been applied to the identification of different calcium phosphate phases of six biologically interesting calcium phosphate phases [61, 62]. Chusuei et al. [61] distinguished between the different samples using the relative PO_3^-/PO_2^- secondary ion ratios in conjunction with XPS quantitative analysis. Later, Lu et al. [62] conducted a principal component analysis of the ToF-SIMS data, which led the authors to the conclusion that a discrimination between the phases can be achieved by comparing the corrected intensities of a few characteristic ions, such as PO_3^-, O^-, Ca^+, PO_2, and OH^-.

The present work, based on the results of a previous feasibility investigation [63], constitutes the first attempt to use ToF-SIMS in conjunction with XPS for discriminating different zinc phosphate chain lengths. Transmission Fourier transform (FT) IR spectroscopy was also used to obtain further proof of the chemical composition and structure of the glasses synthesized in this work.

Experimental

Glass synthesis

Zinc polyphosphates of different chain length were synthesized starting from stoichiometric mixtures of ammonium dihydrogen phosphate (Acros Organics, Geel, Belgium, 99.9% extra pure) and zinc oxide (Alfa Aesar, Karlsruhe, Germany, 99.9%). The reaction for zinc metaphosphate is described in Eq. 1 as an example:

$$2NH_4H_2PO_4 + ZnO \rightarrow 3H_2O + 2NH_3 + Zn(PO_3)_2 \qquad (1)$$

The reagents in powder form were melted in alumina crucibles (high-density alumina produced by Metoxit, Thayngen, Switzerland) at 1,473 K in a 16/3 rotary hearth furnace (Carbolite, Hope Valley, UK) and then quenched in a copper tray that had been previously cooled to 253 K. After quenching, the samples were annealed at 623 K for 5 h to reduce internal stresses.

Four different compositions were investigated: zinc orthophosphate ([P]/[Zn]=2/3), zinc pyrophosphate ([P]/[Zn]=1), zinc metaphosphate ([P]/[Zn]=2), and "zinc

polyphosphate$_{1.5}$" with [P]/[Zn]=3/2 (in this article, "zinc polyphosphate$_{1.5}$" will always refer to this composition).

Sample preparation for surface analysis

The phosphate samples were analyzed by XPS immediately after the annealing step in order to minimize any source of contamination. To investigate the influence of the sample-preparation procedure, a series of metaphosphate samples were also characterized after quenching, after being freshly cleaved, after grinding in an agate mortar, and after mechanical polishing.

The sample-preparation procedure used for the XPS analysis was not ideal for ToF-SIMS experiments. The surface of the samples after quenching was not planar, which resulted in poor sample-charging compensation and, in general, in a low mass resolution. Moreover, the presence of some small copper particles from the copper tray used for the quenching could be detected on the surface and dramatically affected the spectra, increasing their complexity. To improve the quality of the spectra, the samples were mechanically polished prior to ToF-SIMS analysis. Grinding was performed with P320, P600, P1200, and P2400 silicon carbide paper (Presi, Grenoble, France). The subsequent polishing procedure was performed using 3- and 1-μm diamond paste on polishing cloths (Struers, Birmensdorf, Switzerland). Ethanol was always used as a polishing lubricant, in order to remove the heat produced by friction and to minimize chemical changes at the surface. If the samples were too brittle for mechanical polishing (as in the case of zinc orthophosphate), a freshly cleaved area was created outside the sample-introduction chamber immediately before performing the analysis; the analyzed areas were then chosen in regions of the sample that appeared to be relatively flat, and results comparable with those obtained with polished samples were obtained.

Bulk characterization of the glasses

X-ray diffraction (XRD) was used to ascertain that the samples were amorphous. The analyses were performed using an STOE STADI P powder diffractometer (STOE & Cie, Darmstadt, Germany) equipped with an image-plate detector and a Cu Lα X-ray source.

The microelemental analysis for oxygen was performed by means of an RO-478 instrument (Leco, St. Joseph, MI, USA). The phosphorus content was determined by the molybdovanadate method after microwave digestion and subsequent leaching (twice for 50 min) in concentrated sulfuric acid and perchloric acid at 483 and 508 K.

Transmission FT-IR spectra were acquired with a Nicolet™ 5700 FT-IR spectrometer (Thermo Electron Corporation, Madison, WI, USA). The experimental conditions were described in [27]. The glasses were ground with dried KBr and pressed into a pellet. The spectra were processed with OMNIC (version 7.2, Thermo Electron Corporation, Madison, WI, USA). A single-beam spectrum of a bare KBr pellet was acquired before each measurement as a background spectrum.

X-ray photoelectron spectroscopy

The XPS analyses were performed by means of a PHI Quantera SXM spectrometer (ULVAC-PHI, Chanhassen, MN, USA) equipped with an Al Kα monochromatic source, whose beam size ranges from 9 to 200 μm. The Gauze input lenses collect the photoelectrons at an emission angle of 45° and direct them through the high-resolution spherical capacitor analyzer to the 32-channel detector system. The spectrometer is also equipped with a low-voltage argon ion gun and a sample neutralizer for charge compensation. The linearity of the BE scale was checked using sputter-cleaned gold, silver, and copper as reference materials according to ISO 15472:2001. The accuracy was ±0.1 eV. All the experiments were run at residual pressures below 5×10^{-7} Pa. BEs are reported in this work as the means of three or more independent measurements with their corresponding standard deviations.

Survey spectra were acquired in fixed-analyzer-transmission mode, selecting a pass energy of 280 eV, whereas the high-resolution spectra were collected with a pass energy of 26 eV; the full-width at half maximum of the peak-height of the Ag $3d_{5/2}$ signal for high-resolution spectra was 0.62 eV. The beam diameter was 100 μm. The electron neutralizer was used to compensate for sample charging, and the spectra were further corrected with reference to adventitious aliphatic carbon at 285.0 eV.

The spectra were processed using CasaXPS (version 2.3.15, Casa Software, Wilmslow, UK). The background subtraction was performed using the Shirley–Sherwood iterative method [64]. The product of Gaussian and Lorentzian functions was used for the curve-fitting.

The quantitative analysis was performed using the first-principles method valid for homogeneous samples [65]. The inelastic mean free path, λ, was calculated using the TPP-2 M formula [66].

Time-of-flight secondary-ion mass spectrometry

ToF-SIMS spectra were recorded using a ToF-SIMS 5 system (ION-TOF, Münster, Germany) equipped with a bismuth primary ion beam source (acceleration voltage 25 kV) and a low-energy flood gun (acceleration voltage 20 eV) for charge compensation. Each sample was analyzed using Bi_3^{2+} primary ions with a pulsed primary ion current of 0.25 pA and an ion dose of 1×10^{12} ions per square centimeter, which is well

below the static limit for SIMS of 1×10^{13}ions per square centimeter [67]. The beam was set to bunched mode and optimized for high mass resolution. Both negative and positive spectra were acquired with an analyzed area of 200 μm× 200 μm for all experiments.

The spectra were processed using IonSpec (ION-TOF, Münster, Germany). Normalization is a common preprocessing method, and is often used in multivariate analysis of SIMS data, and consists in scaling the data by a constant for each sample This constant could be the intensity of a specific peak, the sum of the intensities of specific peaks, or the total intensity of each sample [65]. When comparing the different samples, we divided the intensity of each peak by the corrected total intensity, which was calculated as the difference between the total intensity and the hydrogen signal intensity.

Results

The phosphates glasses synthesized in this work were clear and transparent, in the shape of round discs, 2–3 cm in diameter and 3–4 mm in thickness. The absence of any peak in the XRD spectra (Fig. S1) confirmed the amorphous state of the samples. The cooling rate necessary to obtain amorphous samples increased with increasing zinc content.

The phosphorus content was determined by microelemental analysis and was compared with the calculated value (Table 1): there was an excellent agreement with the expected phosphorous content for all glasses.

FT-IR analysis

The transmission FT-IR spectra of the zinc phosphate glasses synthesized in the present work are shown in Fig. 2. The IR peaks and the assigned functional groups are listed in Table 2.

As reported in the literature, in the case of phosphate glasses with different compositions [14–18, 43, 68–71], the vibrational spectra of amorphous zinc phosphates are characterized by broad absorption bands in the fingerprint region (2,000–400 cm^{-1}).

The absence of water in the glasses synthesized in the present work is supported by the detection of no bands between 3,600 and 3,400 cm^{-1}, where the O–H stretching vibration of H_2O would be found [72, 73].

In the case of zinc metaphosphate, the asymmetric envelope between 1,350 and 1,200 cm^{-1} (maximum at 1,271 cm^{-1}) is assigned to $\nu_{as}(PO_2^-)$ of Q_2 units and to $\nu(P{=}O)$ of Q_3 units [14, 18, 69]. A contribution to this complex envelope can derive from the characteristic $\nu_s(PO_2^-)$ of Q_2 units, which is usually found as a weak shoulder at approximately 1,160 cm^{-1} [14, 69]. The IR spectra of metaphosphate glasses are usually characterized by a strong band between 820 and 1,050 cm^{-1}, which is assigned to $\nu_{as}(P–O–P)$ of Q_2 units in chain- and ring-type formation [69]. The presence of a peak at 917 cm^{-1} suggests that the tetrahedral units are predominantly arranged in a chain-like structure. The other two bands at 784 and 526 cm^{-1} detected in the FT-IR spectrum of glassy zinc metaphosphate were assigned to the $\nu_s(P–O–P)$ of Q_2 units and to the P-O bending mode, respectively [14, 18, 69].

The absorption bands appearing in the transmission FT-IR spectrum of zinc metaphosphate were also detected in the spectrum of zinc polyphosphate$_{1.5}$, but the peaks exhibited a slight shift (Fig. 2). Moreover, an intense peak was found at 1,134 cm^{-1} and was assigned to the characteristic stretching vibration of Q_1 units, i.e., $\nu_{as}(PO_3^{2-})$.

In the case of glassy zinc pyrophosphate, a complex envelope was also detected in the FT-IR spectrum. The presence of Q_1 units resulted in the appearance of strong absorption bands at 1,122 cm^{-1}, assigned to $\nu_{as}(PO_3^{2-})$, at 932 cm^{-1}, assigned to $\nu_{as}(P–O–P)$, and at 757 cm^{-1}, assigned to $\nu_s(P–O–P)$. Weak peaks at 1,188 cm^{-1}, assigned to $\nu_{as}(PO_2^-)$ of Q_2 units, and at 1,012 cm^{-1}, assigned to $\nu(PO_4^{3-})$ of Q_0 units, were also detected.

As for zinc orthophosphate, the FT-IR spectrum of both the amorphous and the crystalline compound is shown in Fig. 2 for comparison. Compared with the FT-IR spectrum of crystalline zinc orthophosphate, which is characterized by several peaks appearing as a consequence of the change in symmetry induced by the distortion of the tetrahedral orthophosphate anion [74, 75], a broad peak with a maximum at 946 cm^{-1} and a shoulder at higher wavenumbers was

Table 1 Results of the X-ray photoelectron spectroscopy (XPS) quantitative analysis and of the microelemental analysis compared with the composition of the samples investigated calculated from the stoichiometry

	Zinc orthophosphate	Zinc pyrophosphate	Zinc polyphosphate$_{1.5}$	Zinc metaphosphate
XPS[a] (wt%)	[P]=16, [O]=29, [Zn]=55	[P]=23, [O]=36, [Zn]=41	[P]=29, [O]=40, [Zn]=31	[P]=33, [O]=41, [Zn]=26
XPS[a] (at%)	[P]=16, [O]=57, [Zn]=27	[P]=21, [O]=62, [Zn]=17	[P]=24, [O]=64, [Zn]=12	[P]=24, [O]=65, [Zn]=10
Elemental analysis (wt%)	[P]=16.1±0.1	[P]=20.3±0.1	[P]=24.8±0.1	[P]=27.6±0.1
Calculated composition (wt)	[P]=15, [O]=33, [Zn]=50.8	[P]=20.3, [O]=36.8, [Zn]=42.3	[P]=24.7, [O]=40.5, [Zn]=34.8	[P]=27.9, [O]=43.0, [Zn]=29.3

[a] The maximum relative error in the XPS quantitative analysis (calculated as the deviation from the expected value for the less abundant element) is 12%

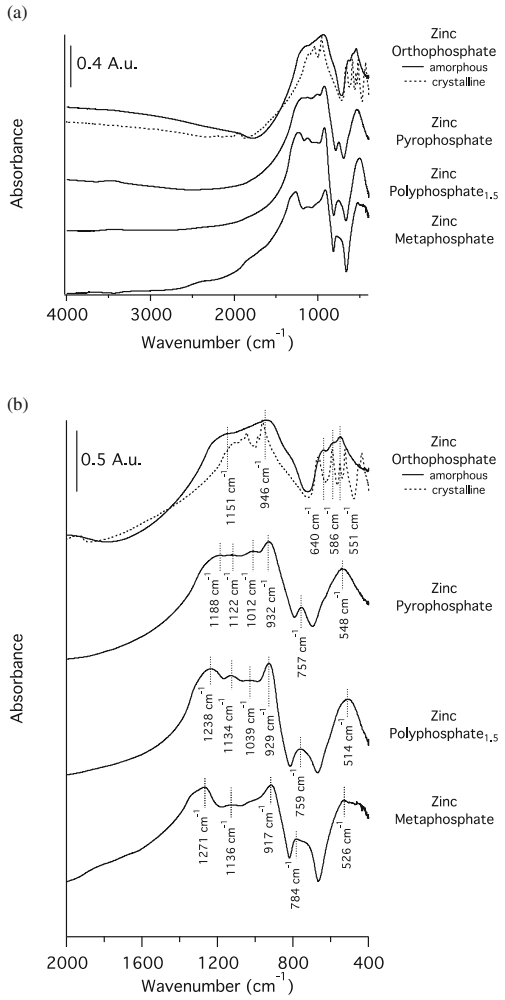

Fig. 2 Transmission Fourier transform in infrared (FT-IR) spectra of zinc phosphate glasses with different compositions (**a**). The FT-IR spectrum of crystalline zinc orthophosphate is shown for comparison. The region at low wavenumbers has been enlarged in (**b**)

detected in the FT-IR spectrum of the amorphous compound, in agreement with the literature [74, 75].

X-ray photoelectron spectroscopy

The survey spectra for all polyphosphate samples are reported in Fig. S2. Similar spectra were obtained for all the glass compositions investigated. The main signals in the spectrum belong to the glass constituents (P, O, Zn). Minor contamination by carbon, arising from the ambient exposure of the samples before analysis, and aluminum, due to the crucibles used for the synthesis, was always observed. The intensity of the C 1*s* peak was always lower than 4% of that of the O 1*s* signal.

High-resolution spectra for the four samples of different composition investigated are depicted in Fig. 3. Moving from the top spectrum to the bottom one in each graph, the ZnO content increases, i.e., the chain length decreases. The possibility of distinguishing phosphate glasses of different chain lengths by XPS is known to be based on the calculation of the ratio between the BO and NBO peaks, which is used for fitting the O 1*s* signal. This procedure has been extensively reported in the literature in the case of both silicate and phosphate glasses [36, 38, 39, 41, 43, 44, 76–78]. In the present work, the O 1*s* signal was fitted with two peaks: the NBO component was found at 532.3±0.1 eV for all samples, whereas the position of the BO turned out to be slightly dependent on the composition. To gain insight into the influence of the ZnO content on the position of the BO peak, the distance between the two peaks was calculated ($\Delta E_{BO/NBO}$). The value of $\Delta E_{BO/NBO}$ was 1.4$_3$ eV for zinc pyrophosphate and 1.6$_7$ eV for zinc metaphosphate. However, the most evident difference between the four spectra was the BO/NBO area ratio; this value decreased from 0.48± 0.02 for zinc metaphosphate to 0.20±0.05 for the zinc pyrophosphate. In the orthophosphate spectra, the BO signal was not detected.

The phosphorus peak was fitted taking into account the spin–orbit coupling with a doublet having one component at lower BE, assigned to the P 2$p_{3/2}$ signal, and one at higher BE,

Table 2 Infrared (IR) frequencies (cm^{-1}) and functional groups for the transmission Fourier transform IR spectra of zinc phosphate glasses with different composition

Frequency (cm^{-1})				Functional group
Zinc metaphosphate	Zinc polyphosphate$_{1.5}$	Zinc pyrophosphate	Zinc orthophosphate	
526	514	548	551 586	δ(P–O)
			640	
784	759	757		ν_s(P–O–P)
917	929	932		ν_{as}(P–O–P)
		1,012	946 1,151 sh	$\nu(PO_4^{3-})$
	1,039			$\nu_s(PO_3^{2-})$
1,136	1,134	1,122		$\nu_{as}(PO_3^{2-})$ and/or $\nu_s(PO_2^-)$
1,271	1,238	1,188		$\nu_{as}(PO_2^-)$ and/or ν(P=O)

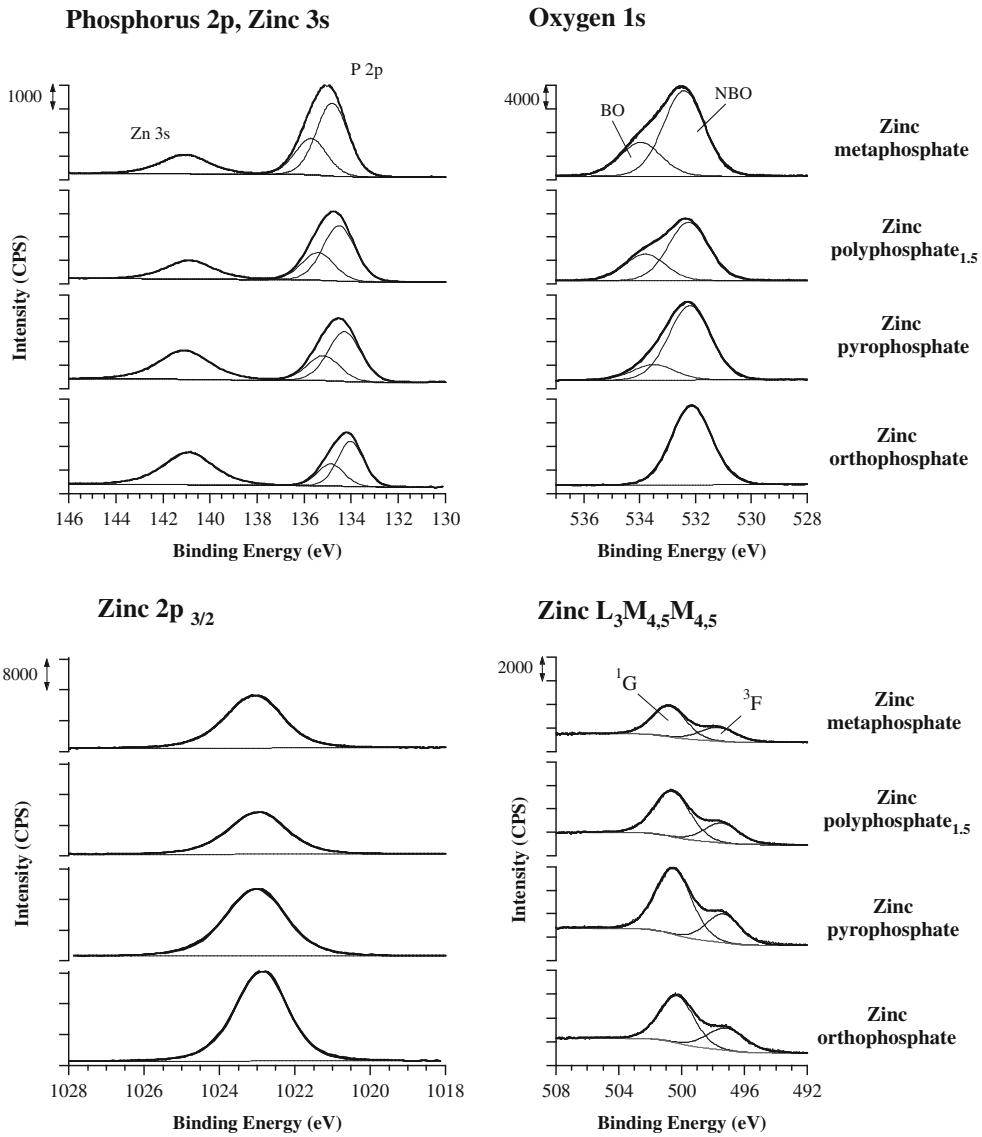

Fig. 3 P 2*p*, Zn 3*s*, O 1*s*, Zn $2p_{3/2}$, and Zn $L_3M_{4,5}M_{4,5}$ high-resolution x-ray photoelectron spectroscopy (XPS) spectra for zinc metaphosphate, zinc polyphosphate$_{1.5}$, zinc pyrophosphate, and zinc orthophosphate

assigned to the P $2p_{1/2}$ signal. The BEs found for metaphosphate glasses (Table 3) are in good agreement with those reported in the literature [38, 39, 43]. The BE of the P 2*p* signal increases when the zinc content decreases (Table 3), in agreement with the finding of Liu et al. [43]: this can be explained by taking into account the fact that the number of PO_2 units increases with chain length, thus increasing the partial positive charge on each phosphorus atom [79].

The Zn 3*s* signal was acquired in the same BE window as that of the P 2*p* signal: it is immediately evident that the P 2*p*/Zn 3*s* area ratio changes with the composition of the glass (see the values in Table 3). Moreover, while the Zn 3*s* peak was not found to shift on changing the glass composition (141.0 eV), the P $2p_{3/2}$ peak shifts gradually from 134.1_0 eV to 134.7_5 eV, moving from the orthophosphate to the metaphosphate composition. The BE difference (ΔBE) between the P $2p_{3/2}$ and P $2p_{1/2}$ signals was 0.8_9 eV. The Zn $2p_{3/2}$ signal was much more intense than the Zn 3*s* signal and its position was also constant at 1,223.0±0.1 eV. The intensities of both Zn 3*s* and Zn $2p_{3/2}$ peaks decrease upon going from orthophosphate to metaphosphate in agreement with the calculated stoichiometry.

Previous publications [80] showed that in the Zn $L_3M_{4,5}M_{4,5}$ region three different final states can be identified, but in our spectra only two signals could be resolved, the ^{1}G and the ^{3}F signals. The position of the most intense peak in the Auger Zn $L_3M_{4,5}M_{4,5}$ region, the ^{1}G signal, shifted from 500.7_7 eV for zinc metaphosphate to 500.3_1 eV for zinc orthophosphate. The ^{3}F signal was at a distance of 3.2 eV on the BE scale. The modified Auger parameter was calculated by adding the BE of the Zn $2p_{3/2}$ signal to the kinetic energy

Table 3 XPS peak binding energies of zinc polyphosphate glasses

	Zinc orthophosphate	Zinc pyrophosphate	Zinc polyphosphate$_{1.5}$	Zinc metaphosphate
O 1*s* NBO (eV)	$532.2_0 \pm 0.1_1$	532.26±0.04	532.28±0.05	532.40±0.09
O 1*s* BO (eV)	-	533.69±0.08	$533.7_1 \pm 0.1_2$	$534.0_7 \pm 0.1_0$
P $2p_{3/2}$ (eV)	134.10±0.09	134.35±0.08	134.49±0.05	134.75±0.08
Zn $2p_{3/2}$ (eV)	1,022.94±0.09	1,023.10±0.04	1,023.01±0.04	$1{,}023.0_4 \pm 0.1_0$
Zn 3*s* (eV)	140.96±0.07	$141.0_5 \pm 0.1_3$	140.94±0.07	141.02±0.09
$ZnL_3M_{4,5}M_{4,5}$ (eV)	500.31±0.05	500.56±0.08	500.61±0.09	$500.7_7 \pm 0.1_4$
P $2p_{1/2}$–P $2p_{3/2}$ BE difference	0.90±0.02	0.90±0.02	0.91±0.02	0.86±0.04
P $2p_{3/2}$/P $2p_{1/2}$ intensity ratio	1.90±0.07	1.84±0.06	$1.7_5 \pm 0.1_0$	$1.7_7 \pm 0.1_5$
BO/NBO intensity ratio	-	0.20±0.05	0.37±0.05	0.48±0.02
P/Zn intensity ratio	0.60±0.08	1.1±0.1	2.0±0.2	2.78±0.6
Zn–P BE difference (eV)	6.86±0.01	6.74±0.09	6.44±0.07	6.19±0.06
Zinc modified Auger parameter, α' (eV)	2009.23±0.09	$2009.1_4 \pm 0.1_0$	2009.00±0.09	$2008.8_7 \pm 0.1_7$
$ZnL_3M_{4,5}M_4$, ^1G–^3F BE difference	3.19±0.03	3.16±0.03	3.18±0.01	3.13±0.02

The maximum error for the binding energies was ±0.1 eV for all signals. The use of a subscript indicates that the digits are given only to avoid loss of information

BO bridging oxygen, *NBO* nonbridging oxygen, *BE* binding energy

(KE) of the Zn $L_3M_{4,5}M_{4,5}$ ^1G signal and was found to shift from 2,008.9±0.1 for zinc metaphosphate to 2009.2±0.1 eV for zinc orthophosphate.

The valence-band region is reported in Fig. 4 and appears to be dominated by a very intense Zn 3*d* peak at 12.5 eV; the Zn 4*s* and O 1*s* signals contribute to the peak found at 6 eV [51]. As observed previously in sodium polyphosphate glasses [81], O 2*s* shows a broad feature at 25 eV, whereas P 3*s* and P 3*p* should appear as a doublet at 14 and 11 eV; the peak at lower BE cannot be clearly resolved from the Zn 3*d* feature, but the P 3*s* peak is observed and its position shifts towards high BEs for the samples with longer chain length.

The results of the quantitative analysis, reported in Table 1, are in agreement with the expected values with a relative error always lower than 12%. The results were similar using either the Zn 2*p* or the Zn 3*s* signal for calculating the atomic percentages. The area ratio, corrected for the appropriate parameters as described in "Experimental," between Zn 3*s* and Zn 2*p* was 1. This result substantiates the assumption that the quantitative analysis is not affected by the presence of carbon on the glass surfaces, which thus can be considered negligible. The values reported in Table 1 were calculated considering the Zn $2p_{3/2}$ signal; this is much more intense than the Zn 3*s* peak, which exhibits a higher signal-to-noise ratio.

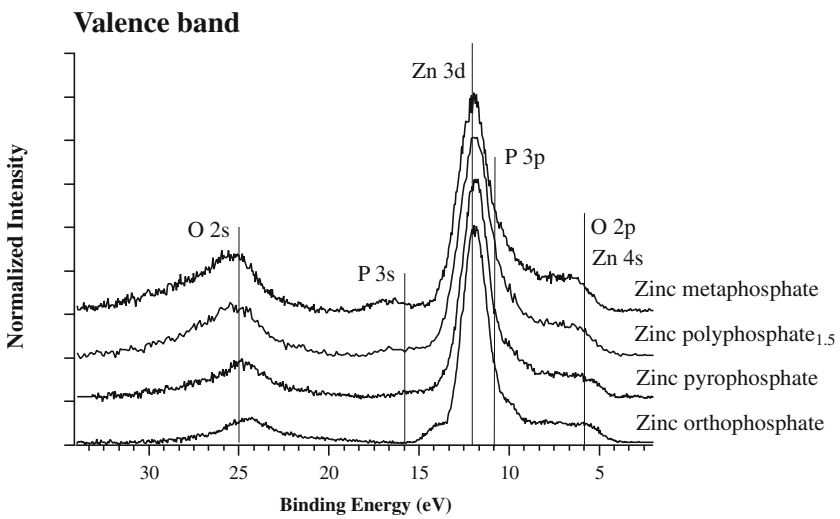

Fig. 4 Valence-band high-resolution XPS spectra after background subtraction for zinc metaphosphate, zinc polyphosphate$_{1.5}$, zinc pyrophosphate, and zinc orthophosphate

However, a closer look at the results reported in Table 1 reveals the presence of a systematic error in the composition obtained by XPS: the measured phosphorus content is always higher than that obtained by elemental analysis. This result led us to hypothesize a difference in composition between the bulk and the surface of the sample. During the cooling of the sample, a gradient in its composition might occur, and to confirm or reject this hypothesis, not only the surfaces but also their cross sections were analyzed together with the pulverized materials or glasses. Cross-sectioning allows XPS analysis in a plane perpendicular to the interface under study, and so differences in the composition might be revealed in that plane. The calculated composition for zinc metaphosphate, reported in Table 4, revealed that the samples had a homogeneous composition: identical results were obtained when analyzing the cross sections and surfaces of the other samples. Only a slight difference in the oxygen content was noticed for the pulverized samples, as expected since they were crushed in air.

Another source of inhomogeneity in the composition could be the degradation of the surface due to hydrolysis. Despite the efforts made to minimize exposure to air, some water could adsorb on the surface and cause depolymerization of the glass and the formation of a compositional gradient. Angular-resolved XPS was performed and showed that the surface of the samples after quenching is homogeneous within the experimental error. The results obtained on zinc metaphosphate are reported as an example in Figs. S3 and S4.

Time-of-flight secondary-ion mass spectrometry

The outcomes of the analyses performed on mechanically polished specimens are reported in Figs. 5 and 6 and are discussed in the following.

A mass resolution ($m/\Delta m$) higher than 7,000 was always achieved for the polished samples, whereas the rough surface of the fractured zinc orthophosphate allowed only a resolution of around 6,000. Figure 5 reports the positive Tof-SIMS spectra for masses up to 200 amu of zinc metaphosphate, zinc pyrophosphate, and zinc orthophosphate. Zinc polyphosphate$_{1.5}$ was also investigated, with analogous results (not shown). In the positive mode the most intense signals were assigned to elements and organic compounds. All spectra show the presence of aluminum, in agreement with the XPS results. The polished samples also indicated slight sodium contamination. The remaining elements detected in the spectra were phosphorus, zinc and its isotopes. The organic fragments were more intense in the spectra of the mechanically polished samples since ethanol was used as a lubricant during polishing. Some typical phosphate fragments (PO^+, PO_3^+) were also detected, but the sensitivity for those peaks was much higher in the negative mode.

The spectra of the samples after quenching were also acquired: they exhibited a mass resolution lower than 5,000, but it was possible to observe the same phosphate fragments and the same trends described here for the mechanically polished samples. The comparison of the polished samples with the nonpolished ones, for both negative and positive polarity spectra, helped in identifying the peaks resulting from the mechanical polishing. Those peaks were mostly organic and did not interfere with the inorganic peaks characteristic of the phosphate glasses.

The negative-ion spectra of the three glasses in a mass range from 10 to 400 amu are shown in Fig. 6. The most intense peaks were assigned to the phosphate fragments PO^-, PO_2^-, PO_3^-, and PO_4^-. At higher masses a typical pattern for the zinc phosphates could be identified, i.e., fragments containing up to four phosphorus atoms with a periodicity of PO_2: $ZnPO_3^-$, $ZnPO_4^-$; $ZnP_2O_6^-$, $ZnP_2O_7^-$; $ZnP_3O_8^-$, $ZnP_3O_9^-$; $ZnP_4O_{11}^-$. This pattern characterizes the spectra of all the glasses investigated, but the relative intensities of these peaks were found to be dependent on the composition. The long-chain-length zinc metaphosphate exhibits higher intensity for all the phosphate-related peaks listed above, especially at high masses ($ZnP_2O_7^-$; $ZnP_4O_{11}^-$).

Table 4 XPS analysis of zinc metaphosphate with different sample preparations

	Zinc metaphosphate after quenching	Zinc metaphosphate freshly cleaved cross section	Zinc metaphosphate pulverized[b]	Zinc metaphosphate mechanically polished
[P][a] (wt%)	33	33	31	31
[O][a] (wt%)	41	41	42	43
[Zn][a] (wt%)	26	26	27	26
BO/NBO intensity ratio	0.48±0.02	0.47±0.05	0.39±0.05	0.39±0.05
P/Zn intensity ratio	2.8±0.6	2.6±0.2	2.5±0.2	2.4±0.2
P–Zn BE difference (eV)	6.19±0.06	6.2±0.1	6.3±0.1	6.3±0.1

[a] The maximum relative error in the XPS quantitative analysis is 12%

[b] The sample was pulverized in air and pressed into a pellet prior to the XPS analysis

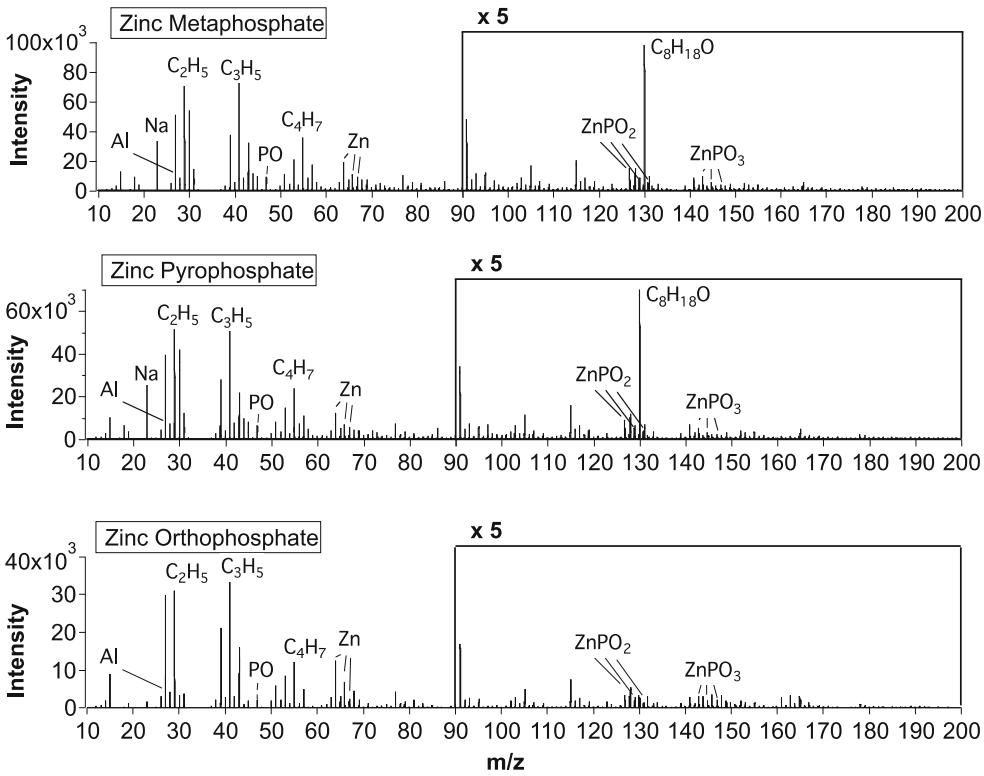

Fig. 5 Positive-ion spectra in the mass range 10–200 amu of zinc metaphosphate, zinc pyrophosphate, and zinc orthophosphate

The spectrum of zinc orthophosphate exhibits additional peaks that can be attributed to zinc oxide and zinc hydroxide: ZnO^-, $ZnOH^-$, ZnO_2^-, ZnO_2H^-, and their isotopes.

In the case of zinc-containing ions, all the corresponding isotopes were always detected. Only the three most intense isotopes (^{64}Zn, ^{66}Zn, ^{68}Zn) are, however, indicated in Fig. 6.

Discussion

Structure and composition of the glasses—bulk analysis

The results of the XRD analysis and of the microelemental analysis demonstrated that the synthesized glasses had the expected composition (Table 1) and structure (i.e., amorphous).

The FT-IR spectra (Fig. 2) of zinc metaphosphate showed the characteristic peaks of glasses with metaphosphate composition, in agreement with previous studies concerning binary amorphous phosphates [14, 18, 69]. Moreover, the absence of a strong absorption band in the region between 1,050 and 1,150 cm^{-1}, where the characteristic stretching vibration of Q_1 units [i.e., $\nu_{as}(PO_3^{2-})$] occurs, indicates that the phosphate tetrahedral structure did not undergo any disproportionation reaction ($Q_2 \rightarrow Q_3+Q_1$), as reported in [18].

Moving from zinc metaphosphate to zinc pyrophosphate, the blueshift and redshift of, respectively, the asymmetric and symmetric P–O–P stretching vibration observed as the amount of ZnO in the phosphate glass increases (Table 2) is in agreement with the literature [82]. However, the structures of glasses whose composition is similar to that of pyrophosphate are known to contain, besides Q_1 units, a certain amount of Q_0 and Q_2 units, which are the products of the disproportionation reaction of Q_1 units ($Q_2 \rightarrow Q_3+Q_1$) [68]. As a consequence of this, the characteristic absorption bands of Q_2 and Q_0 units might contribute to the complex envelopes appearing in the FT-IR spectra of glassy pyrophosphates. The detection of weak peaks, which can be assigned to $\nu_{as}(PO_2^-)$ of Q_2 units and to $\nu(PO_4^{3-})$ of Q_0 units, clearly indicates that the pyrophosphate structure comprised orthophosphate anions as well as a polymeric phosphate chain, suggesting that the pyrophosphate groups indeed underwent a disproportionation reaction.

Phosphorus and zinc chemical state

Few XPS data on zinc binary phosphate glasses in the polyphosphate composition region are available in the literature [38, 39]. These data were acquired with a nonmonochromatic source and under different experimental conditions. As a consequence of this, a direct comparison of the literature data with the present work is difficult. The aim of the previous publications was to investigate the short-range structure of the glasses by studying the oxygen bonding. The current work provides, for the first time, a full characterization of the

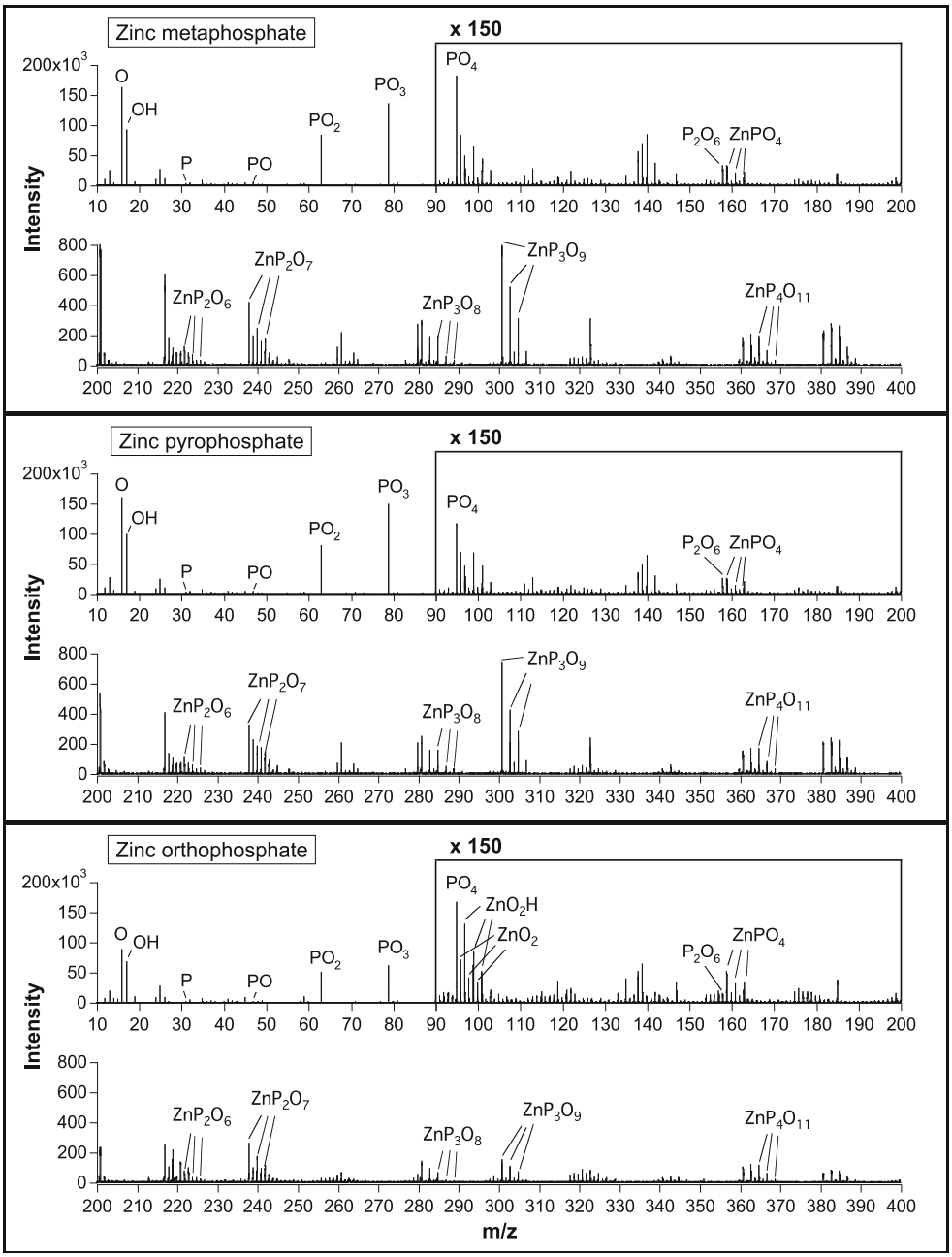

Fig. 6 Negative-ion spectra in the mass range 10–400 amu of zinc metaphosphate, zinc pyrophosphate, and zinc orthophosphate

polyphosphate compositional range (from the metaphosphate long chains to the orthophosphate monomers; see Fig. 1) using a monochromatic source. The aim is to design an analytical strategy that can serve as a basis for an accurate interpretation of more complex spectra such as those of the polyphosphates glasses formed by lubricant additives under extreme high pressures and at high temperatures.

When comparing the absolute BE values obtained from different samples, uncertainties due to the fact that the signals are referred to the C 1*s* peak maximum taken as 285 eV might arise. The amount of carbon present in the sample was very low, and using this very small peak as a reference for the BE scale might have introduced some scatter into the data. Under the assumption that the linearity of the BE scale is maintained, the difference between the BEs of the characteristic signals, $\Delta BE = Zn\ 3s$ - P $2p_{3/2}$, are plotted in Fig. 7. The use of ΔBE (Zn $3s$ – P $2p_{3/2}$) has the advantage of being independent of static-induced uncertainties and, together with the BO/NBO intensity ratio, could also be an effective and diagnostic analytical tool in more complex systems.

In Fig. 8, the BE of the Zn $2p_{3/2}$ signal and the KE of the Auger Zn $L_3M_{4,5}M_{4,5}$ ^1G signal are plotted in a Wagner plot: the straight lines with slope -1 represent the Auger parameter values (α'). Apart from the polyphosphate data, data for metallic zinc, zinc oxide, and zinc sulfide are also plotted in Fig. 8 for comparison. The Wagner plot can be

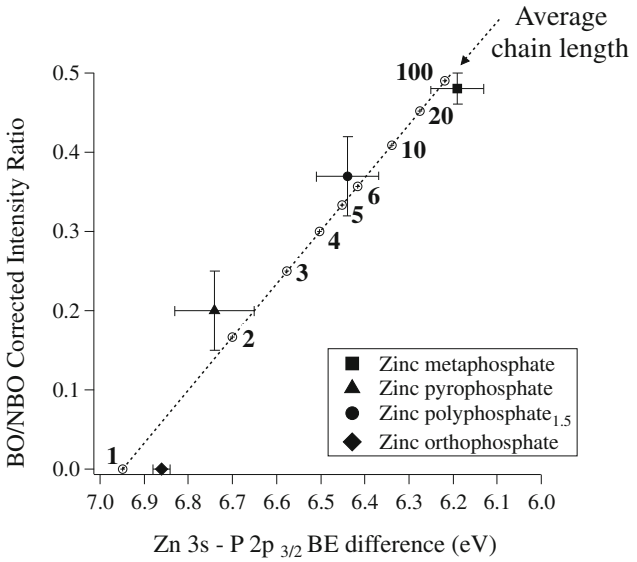

Fig. 7 Bridging oxygen/nonbridging oxygen (*BO/NBO*) intensity ratio versus Zn 3*s*–P $2p_{3/2}$ binding energy (*BE*) difference for zinc polyphosphate glasses of different chain length. The *dotted line* is the result of the correlation between the BO/NBO intensity ratio and Zn 3*s*–P $2p_{3/2}$ BE difference experimental data. The average chain length *n* (*open circles*) was calculated using Eq. 2

used not only to identify chemical states but also to investigate the local chemical environment of the core-ionized atoms, thanks to the recent development of theoretical models based on classical electrostatic and quantum chemistry [53, 54]. As extensively studied by Moretti and Satta [53–55], shifts in the Auger parameter are a direct measure of the polarization energy; assuming that the polarization energy is proportional to the square of the charge and that the BE difference between two core levels is a constant, one can write,

$$\Delta\alpha = 2\Delta R_{ea} \tag{2}$$

where R_{ea} is the extra-atomic relaxation energy, the energy related to the relaxation phenomena occurring outside the ionized atom. Applying this equation to the polyphosphate referred to zinc oxide, we calculate 2.13 eV for zinc orthophosphate, 2.18 eV for zinc pyrophosphate, 2.25 eV for zinc polyphosphate$_{1.5}$, and 2.31 eV for zinc metaphosphate. With an error of ±0.1 eV in the BE and KE, the uncertainty in the estimate of R_{ea} is ±0.14; therefore, we can only state that there is a trend in the data towards lower values of R_{ea} with shorter chain length. These results may indicate that the polyphosphate network becomes more resistant to polarization with increasing chain length. Moreover, the polyphosphates investigated appear in the plot in a vertical line, for which the longer the chain length, the lower the Auger parameter. In this situation, the shift in the Auger parameter is correlated to a change in the Madelung potential. The negative shift of α' going towards longer chain lengths indicates a decrease of the Madelung potential due to the increased covalent character of the compound [53]. With increasing polyphosphate chain length, the electron delocalization on the PO_2 groups also increases, lending stability to the chains but also increasing the positive effective charge at the phosphorus atom [79].

Fig. 8 Wagner plot

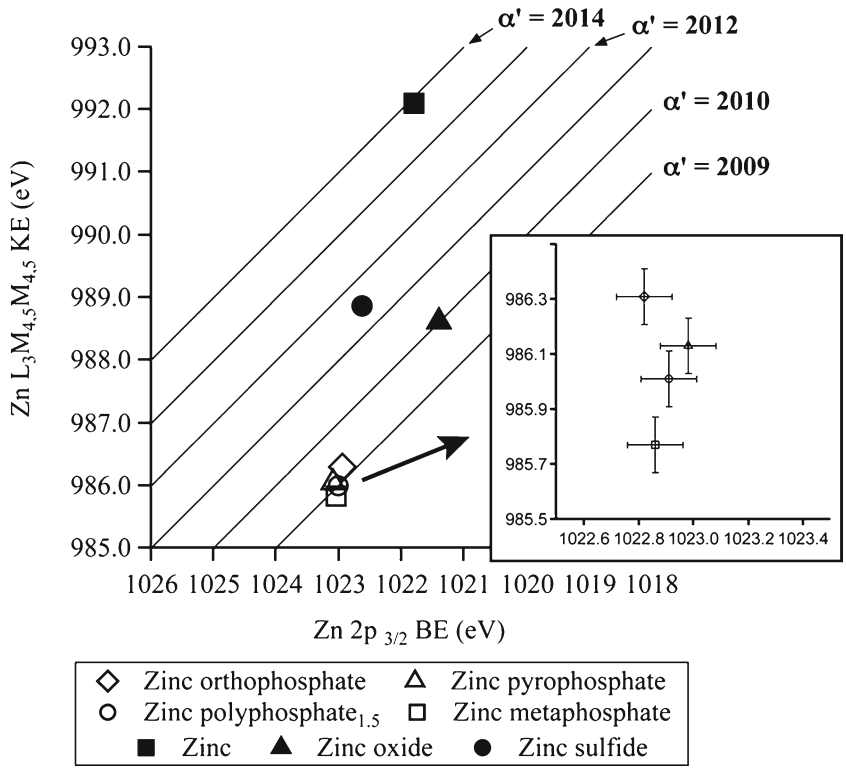

This is confirmed by the valence-band region, where the position of the P 3*s* signal shifts towards high BEs for samples with longer chain length. This result is also consistent with the data for sodium phosphate, where the set of phosphate peaks is even more widely separated for long-chain-length samples [81].

Chain-length determination: the O 1 *s* spectrum and the BO/NBO ratio

It is acknowledged that the addition of a modifying oxide leads to progressive depolymerization of the glass [1, 3, 4]. If one defines the glass with the general formula $x(ZnO)\cdot(1-x)P_2O_5$, the BO/NBO intensity ratio can be calculated from the following equation [37, 38]:

$$BO/NBO = 0.5 \cdot (3 - 4x) \quad (3)$$

The values calculated from this equation are in good agreement with those measured in this work (Table 3). The BEs of both oxygen components move slightly towards lower BEs, implying that the effective nuclear charge of the oxygen atoms in the Q_2 units is higher than that in Q_0 and Q_1 units. The same was also observed for ternary PbO–ZnO–P_2O_5 glasses [43]. The curve-fit of the O 1*s* XPS spectra with two components, one assigned to the NBO and the other to the BO, supports the concept that the two different oxygen atoms in the polyphosphate chains (P=O and P–O–M) cannot be resolved since they have a difference in the BE below the energy resolution achievable here. This finding might be explained by the electronic delocalization on the PO_2^- group. The assignment of the FT-IR absorption bands was also performed on the basis of this evidence: the peak was interpreted as a group vibration, i.e., $\nu(PO_2^-)$ rather than as that of two single and distinct vibrations, i.e., $\nu(P{=}O)$ and $\nu(P{-}O^-)$.

The determination of the chain length of phosphate glasses has been performed on the basis of ^{31}P magic angle spinning NMR spectroscopy in the solid state [6, 83–85] and in solution [3, 7, 13, 14, 78], by high-performance liquid chromatography of dissolved glasses [5], and on the basis of the BO/NBO ratio from curve-fitting of the O 1*s* XPS signal [27, 31, 45, 48].

The BO/NBO ratio calculated from the molar fraction *x* of the ZnO glass modifier according to Eq. 3 is shown in Fig. 9. The decrease of the chain length from metaphosphate (infinite chain length) to the polyphosphate glasses and finally to pyrophosphate (chain length 2) and orthophosphate (chain length 1) is clearly observed. Included in the plot are the experimental data obtained using high-performance liquid chromatography [5].

The ZnO content and the chain length are directly related to the BO/NBO ratio as the number of Q_2, Q_1, and Q_0 units, and thus the number of oxygen atoms in the bridging (BO) and in the nonbridging (NBO) positions changes (see Fig. 1) [2]. The theoretical curve relating the BO/NBO ratio to the chain length is shown in Fig. 10. It can be observed that the BO/NBO ratio is strongly affected at short chain length (from orthophosphate to polyphosphates). However, upon reaching the range of polyphosphate to metaphosphate (chain length greater than 10) the BO/NBO ratio asymptotically approaches the limiting value of 0.5.

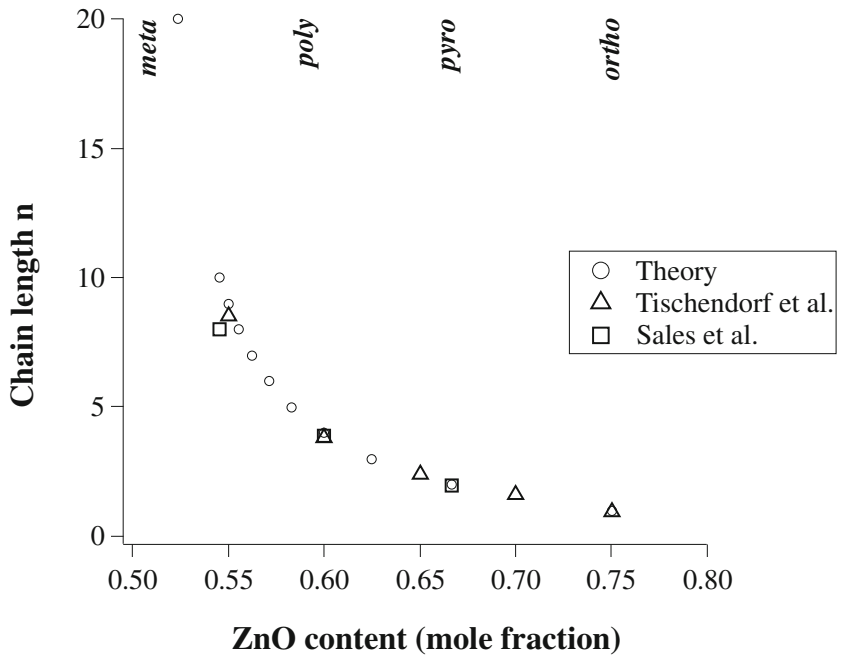

Fig. 9 Calculated (according to theory) average chain length *n* versus the composition of the phosphate glasses (*circles*) in comparison with experimental data from the literature. The data were obtained from high-performance liquid chromatography chromatograms of Tischendorf et al. [5] (*squares*) and Sales et al. [6] (*triangles*)

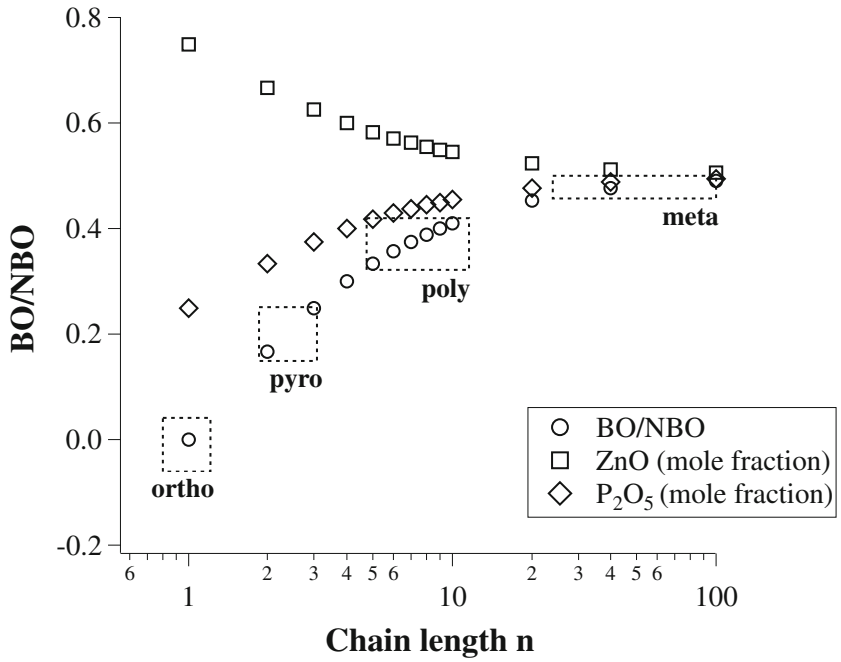

Fig. 10 Calculated BO/NBO ratio versus the chain length *n* of the phosphate glasses (*circles*). Included are the experimental BO/NBO ratio values determined for the four phosphate glasses studied in this work. The *y* height of the *dashed boxes* corresponds to the standard deviations of the BO/NBO value (Table 2); the *x* length is the associated variation in chain length

Concerning chain-length identification in unknown phosphate glassy films based on the experimentally determined BO/NBO ratio with the experimental error (Table 3), it is instructive to examine several specific examples. For a BO/NBO ratio below 0.05, the average chain length is 1, corresponding to orthophosphate. For the experimental BO/NBO value of 0.20±0.05, the average chain length is 1.8–2.5, in good agreement with pyrophosphate. For the experimental BO/NBO value of 0.37±0.05, the chain length can lie between 5 and 15 and for the BO/NBO ratio of 0.48±0.02, the chain length can be anything between 30 and infinity (Fig. 10). Thus, one can conclude that the determination of chain length is more accurate at low values of the BO/NBO ratio.

In addition, as mentioned already, the calculation of the BO/NBO ratio based on experimental O 1 s XPS spectra might be easily affected by the presence of contaminants [86], such as adsorbed water (BE 533 eV), introducing errors in the calculated BO/NBO ratio. Thus, an independent way to determine the chain length is needed. Indeed, on increasing the zinc content in the phosphate glass (and thus decreasing the chain length), the P $2p_{3/2}$ BE decreases (Table 1) and the BE difference between Zn 3*s* and P $2p_{3/2}$ increases (Fig. 7, Table 1). Thus the Zn 3*s*–P $2p_{3/2}$ BE difference might be a better diagnostic analytical tool to determine the chain length in more complex (tribological) systems then the BO/NBO ratio combined with the modified Auger parameter and, when available, the analysis of the valence band. A correlation between the BO/NBO ratio and Zn3*s*–P $2p_{3/2}$ BE difference experimental data and the average chain length *n* calculated using Eq. 2 is plotted in Fig. 7. As a result, the graph can be used to estimate the polyphosphate chain length using the BO/NBO ratio and/or the Zn 3*s*–P $2p_{3/2}$ BE difference.

Composition of the phosphate glasses

To the best of our knowledge, this is the first time that XPS quantitative analysis has been applied to homogeneous polyphosphate glasses. The results (Tables 1 and 4) show a systematic error: the phosphorus content calculated applying the first-principles method is always higher than that measured by elemental analysis. However, the results of the analysis on the cross sections and the pulverized metaphosphate samples (Table 4) confirmed that the samples had a homogeneous composition. A crystalline commercial calcium phosphate was also analyzed and the XPS quantitative results, similarly, showed an overestimation of the phosphorus content compared with the stoichiometric composition (see the electronic supplementary material). The calculated (using the first-principles method) and experimental relative sensitivity factors referred to the P 2*p* peak are reported in Table 5. The explanations for these results could be different. Shirley's algorithm [64] was used as a background subtraction method for this work: this method has the undoubted advantage of being simple and well established, but it omits the shake-up intensities when calculating the peak areas. In some cases those intensities may also significantly vary with chemical state, and such changes would not be taken into account when applying a Shirley background. The use of Tougaard's background subtraction approach [87] could improve the accuracy of the peak areas but would require an acquisition window about five times larger than average (approximately 100 eV instead of approximately 20 eV). Errors may also arise from a wrong estimate of the sensitivity factors using the first-principles method. The values of the photoionization cross-sections, for example, were calculated by Scofield [88] using

Table 5 Calculated and experimental relative sensitivity factors referred to the P 2*p* peak

Peak 1	Peak 2	Compound	S_1/S_2	
			Experimental	First-principles method
O 1*s*	P 2*p*	Zinc metaphosphate	1.411	1.745
O 1*s*	P 2*p*	Zinc polyphosphate	1.477	1.749
O 1*s*	P 2*p*	Zinc pyrophosphate	1.480	1.748
O 1*s*	P 2*p*	Zinc orthophosphate	1.545	1.749
Zn 2*p*	P 2*p*	Zinc metaphosphate	5.972	7.812
Zn 2*p*	P 2*p*	Zinc polyphosphate	5.942	7.869
Zn 2*p*	P 2*p*	Zinc pyrophosphate	6.499	7.877
Zn 2*p*	P 2*p*	Zinc orthophosphate	6.883	7.888
Zn 3*s*	P 2*p*	Zinc metaphosphate	0.480	0.756
Zn 3*s*	P 2*p*	Zinc polyphosphate	0.511	0.756
Zn 3*s*	P 2*p*	Zinc pyrophosphate	0.575	0.755
Zn 3*s*	P 2*p*	Zinc orthophosphate	0.627	0.755

the Hartree–Slater model, which is inaccurate because of its approximate manner of treating the electron–electron interactions. Nevertheless, Scofield's cross sections are still the most accurate values available today [89]. Whatever the source of the error, it is evident that great care should be taken when investigating polyphosphates using quantitative XPS. Experimental sensitivity factors calculated directly from a reference compound should be used whenever possible.

ToF-SIMS analysis

A characteristic "fingerprint" composed of phosphate fragments was identified in the negative-mode spectra of all the glasses. The absence of contaminant elements in the positive spectra was essential in order to be able to confirm the assignment of the peaks in the negative spectra. Comparison with the spectra of the samples before mechanical polishing was also used to identify the peaks arising from the solvent used during the polishing step.

In the second part of the data processing, the "fingerprint" fragments in the spectra of the different glasses investigated were compared. The corrected intensities of those fragments for three polyphosphates of different chain lengths (zinc metaphosphate, zinc pyrophosphate, and zinc orthophosphate) are reported in Fig. 11. Different normalization methods were applied to the data, based on the total intensity, on the sum of selected peaks, and on the P^- signal intensity corrected by the stoichiometry. The normalized data always showed the same trend in all cases, but the normalization based on total intensity was the most effective method for removing variations induced by topography, sample charging, and experimental conditions [90]. The PO_2^- and PO_3^- fragments were been considered in this comparison because their intensity was so high that the saturation limit of the analyzer could have been reached. The spectrum of the orthophosphate was unequivocally identified by the presence of the fragments related to the

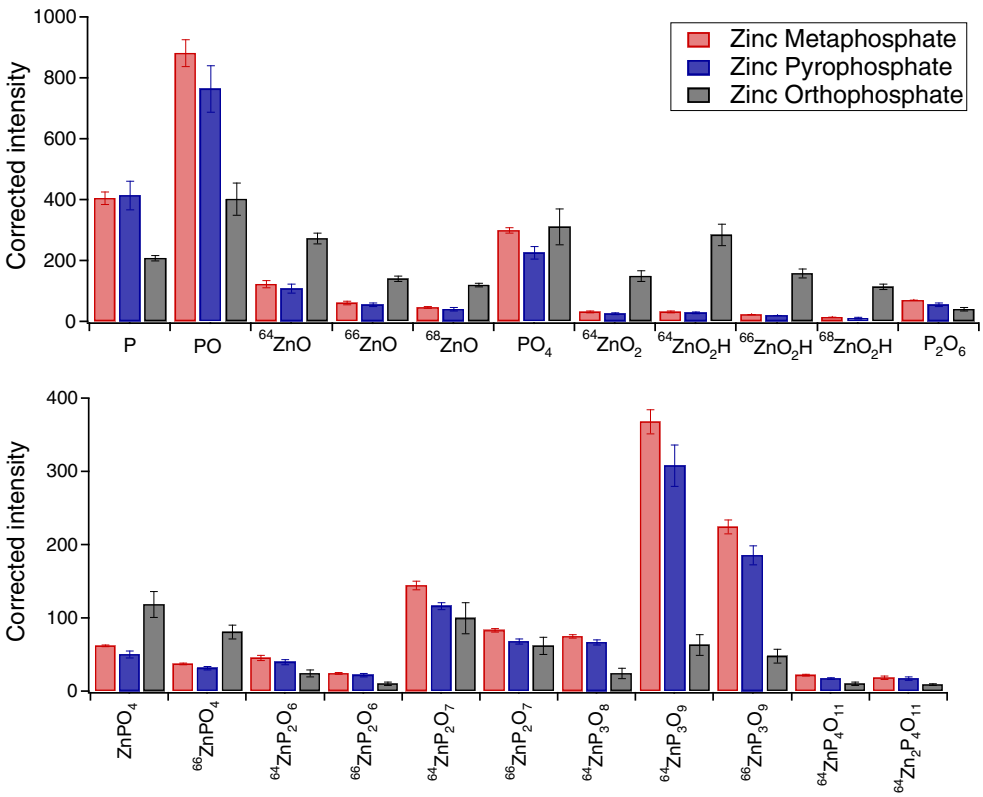

Fig. 11 Comparison between the corrected intensities of the characteristic time-of-flight secondary-ion mass spectrometry signals of zinc metaphosphate, zinc pyrophosphate, and zinc orthophosphate

zinc oxide/zinc hydroxide. Moreover, the intensity of the phosphorus-containing fragments is lower for the orthophosphate, except for the peaks containing PO_4 (PO_4, $ZnPO_4$ and its isotopes). This is consistent with the FT-IR results that show that the orthophosphate is mainly formed by Q_0 tetrahedra.

Zinc pyrophosphate and zinc metaphosphate are characterized by the same fragments and can be distinguished by taking into account the differences in intensities of the phosphate fragments. The phosphate peaks, especially at high masses ($ZnP_2O_7^-$ and $ZnP_3O_9^-$), exhibit lower intensities in the case of zinc pyrophosphate (see Fig. 11). In the pyrophosphate composition, as also shown by FT-IR spectroscopy, the glass undergoes a disproportionation reaction, with the consequence that some Q_0 and Q_2 tetrahedra coexist with the Q_1 tetrahedra. This phenomenon was not detected by the XPS measurements because the calculated BO/NBO intensity ratio provides an averaged chain length. However, the ToF-SIMS spectra are certainly affected by the local structure of the samples. This difference might help in explaining the absence of any clear difference between metaphosphate and pyrophosphate spectra. Another difference with the XPS measurements is the sample preparation (see "Bulk characterization of the glasses"). The surface of the mechanical polished samples was also characterized by XPS (see Table 4 for the case of zinc metaphosphate). The BO/NBO ratio decreases from 0.45±0.05 for the sample analyzed after quenching to 0.39±0.05 for the mechanically polished zinc metaphosphate, whereas the Zn 3*s*–P $2p_{3/2}$ BE difference increases from 6.2±0.1 eV to 6.3±0.1 eV. These results suggest a slight depolymerization, within experimental error, of the glass in comparison with the samples analyzed after the quenching. The same trend was observed in the samples pulverized in air and indicates that the mechanical stress induces changes in the glass composition.

ToF-SIMS has already been employed for differentiating between calcium phosphate phases. Also in this case selected peaks were discriminated and used as a fingerprint for identification of the CaP phases [61, 62].

The method described here has some limitations in practical applications, for example, with a mixture of compounds. The stability of the method in the presence of contaminants should also be explored. The use of statistical methods, such as principal component analysis, could be applied in the future to help interprete such complex spectra.

Conclusions

A method for the discrimination of zinc polyphosphate glasses of different chain lengths by means of surface-analytical tools has been described. A foundation of systematic studies on the pure compounds is essential when applying these same techniques to more complex systems. ToF-SIMS and XPS appear to be well suited for the investigation of such systems:

- The combined use of the BO/NBO intensity ratio, the Zn 3*s*–P $2p_{3/2}$ BE difference, and the modified Auger parameter allows unambiguous differentiation between four samples with composition ranging from zinc orthophosphate, formed by PO_4 monomers, to zinc metaphosphate, which is characterized by a long-chain structure.
- ToF-SIMS was also shown to be a powerful method for successfully discriminating the phosphates of different chain lengths by comparing the corrected intensities of the phosphate fragments. Zinc orthophosphate can be differentiated by the presence of peaks attributed to zinc oxide and zinc hydroxide; moreover the PO_4^- and $ZnPO_4^-$ fragments show a higher corrected intensity, compared with samples with longer chain lengths. Zinc pyrophosphate shows the same fragments as zinc metaphosphate but the intensity of the phosphate peaks is lower, especially at higher masses, ($ZnP_2O_7^-$, $ZnP_3O_9^-$).

These surface-analytical methods, alone or in combination, can thus provide a powerful tool for basic research in fields, such as tribology, where the surface chemistry of polyphosphates can play a key role.

Acknowledgements The authors would like to thank Karl-Emanuel Mayerhofer, Peggy Rossbach, and Beat Keller from the Empa Laboratory for Nanoscale Materials Science (Dübendorf, Switzerland) for their support and experimental help with ToF-SIMS. M. Schneider kindly performed the microelemental analysis. This research was funded by the ETH Research Commission. A.R. thanks the Università di Cagliari for its support.

References

1. Martin SW (1991) Eur J Solid State Inorg Chem 28:163–205
2. Brow RK (2000) J Non-Cryst Solids 263–264:1–28
3. Brow RK, Tallant DR, Myers ST, Phifer CC (1995) J Non-Cryst Solids 191(1–2):45–55
4. Van Wazer JR (1958) Phosphorus and its compounds, vol 1. Interscience Publishers, New York
5. Tischendorf B, Otaigbe JU, Wiench JW, Pruski M, Sales BC (2001) J Non-Cryst Solids 282(2–3):147–158
6. Sales BC, Otaigbe JU, Beall GH, Boatner LA, Ramey JO (1998) J Non-Cryst Solids 226(3):287–293
7. Wiench JW, Tischendorf B, Otaigbe JU, Pruski M (2002) J Mol Struct 602:145–157
8. Walter G, Hoppe U, Vogel J, Carl G, Hartmann P (2004) J Non-Cryst Solids 333:252–262
9. Hoppe U, Walter G, Carl G, Neuefeind J, Hannon AC (2005) J Non-Cryst Solids 351(12–13):1020–1031
10. Musinu A, Piccaluga G, Pinna G, Narducci D, Pizzini S (1989) J Non-Cryst Solids 111(2–3):221–227
11. Musinu A, Piccaluga G (1995) J Non-Cryst Solids 192–193:32–35
12. Bionducci M, Licheri G, Musinu A, Navarra G, Piccaluga G, Pinna G (1996) J Phys Sci 51(12):1209–1215

13. Lai A, Musinu A, Piccaluga G, Puligheddu S (1997) Phys Chem Glasses 38(4):173–178
14. Meyer K (1997) J Non-Cryst Solids 209(3):227–239
15. Bartholomew RF (1972) J Non-Cryst Solids 7(3):221–235
16. Dayanand C, Bhikshamaiah G, Tyagaraju VJ, Salagram M, Krishna Murthy ASR (1996) J Mater Sci 31(8):1945–1967
17. Schwarz J, Ticha H, Tichy L, Mertens R (2004) J Optoelectron Adv Mater 6(3):737–746
18. Velli LL, Varsamis CPE, Kamitsos EI, Moncke D, Ehrt D (2005) Phys Chem Glasses 46(2):178–181
19. Brow RK, Click CA, Alam TM (2000) J Non-Cryst Solids 274:9–16
20. Takebe H, Baba Y, Kuwabara M (2006) J Non-Cryst Solids 352 (28–29):3088–3094
21. Abou Neel EA, Pickup DM, Valappil SP, Newport RJ, Knowles JC (2009) J Mater Chem 19(6):690–701
22. Muresan D, Dragan Bularda M, Popa C, Baia L, Simon S (2004) Structural and biological investigation of phosphate glasses with silver. Biophys Environ Phys 2004:232–237
23. Marasinghe GK, Karabulut M, Ray CS, Day DE, Shumsky MG, Yelon WB, Booth CH, Allen PG, Shuh DK (1997) J Non-Cryst Solids 222:144–152
24. Spikes H (2004) Surface chemistry in tribology. Tribol Lett 17 (3):469–489
25. Gellman A, Spencer N (2002) Proc Inst Mech Eng Part J J Eng Tribol 216(6):443–461
26. Martin J (1999) Tribol Lett 6(1):1–8
27. Crobu M, Rossi A, Mangolini F, Spencer ND (2010) Tribol Lett 39 (2):121–134
28. Gauvin M, Dassenoy F, Belin M, Minfray C, Guerret-Piecourt C, Bec S, Martin JM, Montagnac G, Reynard B (2008) Tribol Lett 31 (3):139–148. doi:10.1007/S11249-008-9346-X
29. Mangolini F (2011) Reactivity of environmentally compatible lubricant additives: an In Situ and Ex Situ Investigation; PhD Thesis No. 19677, ETH Zürich, Zurich
30. Eglin M, Rossi A, Spencer ND (2003) Tribol Lett 15(3):199–209
31. Martin JM, Grossiord C, Le Mogne T, Bec S, Tonck A (2001) Tribol Int 34(8):523–530
32. Zhang Z, Yamaguchi ES, Kasrai M, Bancroft GM, Liu X, Fleet ME (2005) Tribol Lett 19(3):221–229
33. Scorciapino MA, Navarra G, Elsener B, Rossi A (2009) J Phys Chem C 113(51):21328–21337. doi:10.1021/jp906326m
34. Rossi A, Elsener B (1992) Surf Interface Anal 18(7):499–504. doi:10.1002/sia.740180708
35. Franke R, Hormes J (1995) Physica B 216(1–2):85–95. doi:10.1016/0921-4526(95)00446-7
36. Bruckner R, Chun HU, Goretzki H, Sammet M (1980) J Non-Cryst Solids 42(1–3):49–60
37. Gresch R, Müller-Warmuth W, Dutz H (1979) J Non-Cryst Solids 34:127–136
38. Brow RK (1996) J Non-Cryst Solids 194(3):267–273
39. Onyiriuka EC (1993) J Non-Cryst Solids 163:268–273
40. Chowdary BVR, Tan KL, Chia WT, Gopalakrishnan R (1990) J Non-Cryst Solids 119:95–102
41. Smets BMJ, Krol DM (1984) Phys Chem Glasses 25(5):113–118
42. Brow RK, Arens CM (1993) Phys Chem Glasses 35(3):132–199
43. Liu HS, Chin TS, Yung SW (1997) Mater Chem Phys 50(1):1–10
44. Shih PY, Yung SW, Chin TS (1999) J Non-Cryst Solids 244(2–3):211–222
45. Heuberger R, Rossi A, Spencer ND (2007) Pressure dependence of ZnDTP tribochemical film Formation: a combinatorial approach 28 (2):209-222
46. Heuberger R, Rossi A, Spencer ND (2007) Tribol Lett 25(3):185–196
47. Piras FM, Rossi A, Spencer ND (2003) Tribol Lett 15(3):181–191
48. Rossi A, Piras FM, Kim D, Gellman AJ, Spencer ND (2006) Tribol Lett 23(3):197–208
49. Brow RK (1989) J Vac Sci Technol 7(3):1673–1676
50. Briggs D (2003) In: Briggs D, Grant JT (eds) Surface analysis by Auger and X-ray photoelectron spectroscopy. IM Publications, Trowbridge
51. Wagner CD, Joshi A (1988) J Electron Spectrosc 47:283–313
52. Gaskell KJ, Smith MM, Sherwood PMA (2004) Valence band x-ray photoelectron spectroscopic studies of phosphorus oxides and phosphates. J Vac Sci Technol A Vac Surf Films 22(4):1331–1336. doi:10.1116/1.1763904
53. Moretti G (1998) J Electron Spectrosc 95:95–144
54. Moretti G (1995) J Electron Spectrosc 76:365–370
55. Satta M, Moretti G (2010) J Electron Spectrosc 178–179:123–127. doi:10.1016/j.elspec.2009.07.008
56. Smith GC, Bell JC (1999) Appl Surf Sci 144–145:222–227
57. Rossi A, Eglin M, Piras FM, Matsumoto K, Spencer ND (2004) Wear 256(6):578–584. doi:10.1016/J.Wear.2003.10.001
58. Minfray C, Martin JM, De Barros MI, Le Mogne T, Kersting R, Hagenhoff B (2004) Tribol Lett 17(3):351–357
59. Minfray C, Martin JM, Esnouf C, Le Mogne T, Kersting R, Hagenhoff B (2004) Thin Solid Films 447–448:272–277
60. Murase A, Ohmori T (2001) Surf Interface Anal 31(2):93–98
61. Chusuei CC, Goodman DW, Van Stipdonk MJ, Justes DR, Schweikert EA (1999) Anal Chem 71(1):149–153
62. Lu HB, Campbell CT, Graham DJ, Ratner BD (2000) Anal Chem 72(13):2886–2894. doi:10.1021/Ac990812h
63. Pinna R (2001/2002) Synthesis and characterization of Zn and Fe polyphosphates glasses. Diploma thesis, University of Cagliari
64. Shirley DA (1972) High-resolution x-ray photoemission spectrum of valence bands of gold. Phys Rev B 5(12):4709-4714
65. Seah MP (1990) Quantification of AES and XPS, in practical surface analysis. Wiley, Chichester
66. Tanuma S, Powell CJ, Penn DR (1994) Surf Interface Anal 21 (3):165–176
67. Van Vaeck L, Adriaens A, Gijbels R (1999) Mass Spectrom Rev 18 (1):1–47. doi:10.1002/(sici)1098-2787(1999)18:1<1::aid-mas1>3.0.co;2-w
68. Efimov AM (1997) J Non-Cryst Solids 209(3):209–226
69. Rulmont A, Cahay R, Liegeoisduyckaerts M, Tarte P (1991) Eur J Solid State Inorg Chem 28(1):207–219
70. Shih PY (2003) Mater Chem Phys 80(1):299–304
71. Termine JD, Lundy DR (1974) Calcif Tissue Rese 15(1):55–70
72. Colthup NB, Daly LH, Wiberley SE (1990) Introduction to infrared and Raman spectroscopy, 3rd edn. Academic, New York
73. Socrates G (2001) Infrared and Raman characteristic group frequencies, 3rd edn. Wiley, Chichester
74. Chen WS, Monroe EA, Condrate RA, Guo YM (1993) J Mater Sci Mater Med 4(2):111–116
75. Crisp S, Oneill IK, Prosser HJ, Stuart B, Wilson AD (1978) J Dent Res 57(2):245–254
76. Khawaja EE, Durrani SMA, Aladel FF, Salim MA, Hussain MS (1995) J Mater Sci 30(1):225–234
77. Salim MA, Khattak GD, Fodor PS, Wenger LE (2001) J Non-Cryst Solids 289(1–3):185–195
78. Flambard A, Videau JJ, Delevoye L, Cardinal T, Labrugere C, Rivero CA, Couzi M, J (2008) Structure and nonlinear optical properties of sodium-niobium phosphate glasses. Non-Cryst Solids 354(30):3540–3547. doi:10.1016/j.jnoncrysol.2008.03.017
79. Beletskii IP, Yatsimirskii KB (1988) Theor Exp Chem 23(6):621–627. doi:10.1007/bf00534602
80. Antonides E, Janse EC, Sawatzky GA (1977) Phys Rev B 15 (10):4596
81. Gaskell KJ, Asunskis AL, Sherwood PMA (2002) Surf Sci Spectra 9(1):151–158. doi:10.1116/11.20030114

82. Karabulut M, Metwalli E, Day DE, Brow RK (2003) J Non-Cryst Solids 328(1–3):199–206
83. Le Saout G, Simon P, Fayon F, Blin A, Vaills Y (2002) J Raman Spetrosc 33(9):740–746. doi:10.1002/jrs.911
84. Le Saout G, Fayon F, Bessada C, Simon P, Blin A, Vaills Y (2001) J Non-Cryst Solids 293:657–662
85. Qiu D, Guerry P, Ahmed I, Pickup DM, Carta D, Knowles JC, Smith ME, Newport RJ (2008) Mater Chem Phys 111(2–3):455–462
86. Mangolini F, Rossi A, Spencer ND (2011) J Phys Chem C 115 (4):1339–1354. doi:10.1021/jp107617d
87. Pauly N, Tougaard S (2010) Surf Sci 604(13–14):1193–1196. doi:10.1016/j.susc.2010.04.001
88. Scofield JH (1976) J Electron Spectrosc 8(2):129–137
89. Seah MP, Gilmore IS (2006) Phys Rev B 73(17)174113
90. Vickerman JC (1997) In: Vickerman JC (ed) Surface analysis - the principal techniques. Wiley, Chichester. pp 564–612